SUPPLEMENTARY INFORMATION: Three-dimensional entanglement on a silicon chip

Liangliang Lu[1,†], Lijun Xia[1,†], Zhiyu Chen[1,†], Leizhen Chen[1], Tonghua Yu[1], Tao Tao[1],

Wenchao Ma[1], Ying Pan[2], Xinlun Cai[2], Yanqing Lu[1], Shining Zhu[1], Xiao-Song Ma[1,*1]

[1] [1] National Laboratory of Solid-state Microstructures,

School of Physics, College of Engineering and Applied Sciences,

Collaborative Innovation Center of Advanced Microstructures, Nanjing University, Nanjing 210093, China

[2] State Key Laboratory of Optoelectronic Materials and Technologies and School

of Physics and Engineering, Sun Yat-sen University, Guangzhou 510275, China

[†]These authors contributed equally to this work

[*]e-mail:Xiaosong.Ma@nju.edu.cn

1 Supplementary notes

Details of the silicon device and experiment

A schematic of the experimental setup is shown in Supplementary Figure 1. The components used in the experiment are all commonly used components for C-band wavelengths. Photon pairs are generated by coupling the pump light into the resonator using spontaneous four wave mixing (SFWM). Then the asymmetric Mach-Zehnder interferometer (AMZI) with a length difference of 47μm is used as an on-chip wavelength division multiplexer (WDM) to split the signal and idler photons into two multi-port interferometers. In our case, the free spectral range (FSR) is approximately 12 nm, which introduces a 3 dB filtering loss for both the signal and idler photons when they are divided into the two output ports of the AMZI in the path correlation measurements. In the time-reversed Hong-Ou-Mandel (RHOM) measurements, we do not use the WDM to separate the signal and idler photons. Therefore, the RHOM interference counts (interference on one side) are approximately four times larger than the correlation counts in the main text. After a local reconfigurable manipulation, the photons are coupled out of the chip for detection. The chip is mounted on a stage and wire-bonded on a printed circuit board (PCB) for electrical contact.

The device is a silicon-on-insulator (SOI) chip fabricated using 248 nm deep-UV lithography at the advanced micro foundry (AMF) with 220 nm top thickness on 2 μm buried oxide. The waveguides are 500 nm wide and covered with a 2.8 μm silicon dioxide upper cladding. Resistive heaters are patterned as thermo-optic phase shifters (PSs) on a 120 nm thick TiN metal layer and placed 2 μm above the waveguide layer. To change the phase, we change the current propagating through the TiN metal

layer to heat the waveguide and then change the refractive index. Multi-mode interferometers (MMIs) are used as beam-splitters with near 50:50 splitting ratio in the on-chip WDM and MZIs (see Fig. 1 of the main text).

The photon pair generation source is designed with two pulley-type waveguides wrapped around the ring, essentially establishing two unbalanced MZIs. The ring has a radius of 15 μm and a coupling gap of 250 μm (200 μm) at the input (output) side. The length difference of the unbalanced MZI1 (MZI2) is 47.8 μm (48 μm) and its sinusoidal spectrum determines the wavelength of the constructive and destructive interference. Supplementary Figure 2 shows the pump resonance transmission spectra of source1 (S1), source2 (S2) and source3 (S3) with full widths at half maximum of 44 pm, 50 pm and 53 pm. The resonance splitting of S2 and S3 are due to surface-roughness-induced backscattering [1].

To pump the sources, laser pulses are produced by a tunable picosecond fibre laser at 1552.02 nm (pulse duration of 7.8 ps, repetition rate of 60.2 MHz, and average power of -0.8 dBm). Before coupling the pump pulse into the chip, the unwanted amplified spontaneous emission (ASE) noise of the pump is filtered by a WDM (extinction ratio of $\sim$40 dB and a bandwidth of 1.2 nm) and the polarization of the pump is optimized for maximum fibre-to-chip coupling by a polarization controller (PC). A 32-channel V groove fibre array with a spacing of 127 μm and polishing angle of 10^0 is used to couple the light via transverse electric (TE) grating couplers into the chip. The FSR of the source is approximately 6.2 nm. Entangled photons emerging from the chip are filtered by off-chip single-channel WDMs to remove the residual pump and are finally detected by six superconducting nanowire single photon detectors (SSPD) with 80% detection efficiency, 100 Hz dark count rates, a 50 ns dead time and a 100 ps timing jitter. The losses for the photons in the path entanglement measurement add up to 18.73 dB $\sim$ 19.13 dB, which can be decomposed as follows: the total fibre-chip-fibre loss is 15.56 dB (measured by launching non-resonance light of 1 mW and collecting the output power at the through port of the source), the insertion losses over the full band of the off-chip WDMs are 2-2.4 dB, and the detection losses are 0.97 dB. The detector electrical signals are collected by a field-programmable gate array (FPGA)-based timetag device. All the heaters are independently controlled by a programmable current source with a range of 0-20 mA and 16-bit resolution. **Crosstalk** Mitigating the electrical and thermal crosstalk within hundreds of micrometres is one of the main challenges in our experiment. The relative distances between each component are shown in Supplementary Figure 3a. To reduce the number of electrical pads, we designed all the heaters to have a common ground. However, the resistance between the common ground and true ground is not necessarily zero due to the electrical crosstalk. There are several ways to effectively avoid this effect such as a pre-processing method [2], a passive compensation method [3], a negative feedback scheme [4], equipping each heater with two separate pads (one for the signal and one for the ground) and using current output equipment [5]. We tried to use negative feedback to minimize the electrical crosstalk effect. However, as the number of heaters working simultaneously increases, it becomes increasingly difficult to optimize the feedback system to the

precision. As shown in Supplementary Figure 3b, we measure the pump transmission spectrum of source 1 (S1) from the input port to the through port of the resonator with and without applying voltages to the other heaters. We choose two heaters (I_{z2} and S_{z3}) with approximately equal resistances. When the voltage (4.303 V) is applied to I_{z2} or S_{z3}, a common ground voltage (V_G) arises due to the resulting current passing through the contact resistance between the on-chip gold pad and wire-bonded contacts. The effective voltages (heating power) applied to the source are then reduced, resulting in a smaller effective refractive index (n_{eff}) change of the waveguide. The change in n_{eff} as a function of temperature can be expressed as $\frac{dn}{dT}\Delta T$, where $\frac{dn}{dT}$ is the thermo-optic coefficient and ΔT is the change in temperature. The thermal-optic coefficient of silicon at 300 K near 1550 nm is $1.86 \times 10^{-4} K^{-1}$ [6]. Optical resonances in a resonator require that the optical length (n_{eff}L, where L is the round-trip length) is a multiple of the wavelength of the light. Hence, the reduction in n_{eff} leads to the blueshift of the resonance wavelength. In Supplementary Figure 3b, the resonance wavelength blueshifts 15 pm when the voltage is applied to I_{z2} or S_{z3}. The two approximately equal resistances with the same applied voltages provide similar electrical crosstalk, so the blue and green curves in Supplementary Figure 3b overlap well. We finally chose to use the current source, which is suitable for our experiment.

The thermal crosstalk originating from the heat transfer between the thermos-optical PSs also plays an important role. When we adjust the PSs of the WDMs and the multi-port interferometers, the thermal crosstalk poses a significant challenge for the spectral alignment of different sources due to the narrow resonance linewidths of our resonator-based sources. To overcome this challenge, we optimize the heat sink of the chip carrier and the design of the chip. We quantify the thermal crosstalk with and without (W.O.) heating the PSs with different distances to the source. The heating power is set to 20 mW. Supplementary Figure 3c shows that when the distance between the heater and the resonator decreases, there will be an obvious redshift due to the thermal crosstalk. As can be seen from the figure, the resonance of S1 shifts approximately 5 pm when the heater is positioned at a distance of 500 μm from S1, while for a distance of 1200 μm, there is little influence due to the thermal crosstalk. In our design, we distanced the PS that needs to be adjusted and the nearest source and achieved a desired isolation level. From the interference fringes shown in Fig. 2 in the main text, we note that the heat diffusion from the PSs has little effect on the sources within a power change of 0~42 mW (2π phase).

Theoretical analysis and experimental characterization of the dual Mach-Zehnder interferometer micro-ring (DMZI-R) source on a chip

We employ a quadruple-coupler ring resonator with the scheme presented in Supplementary Figure 4a, which is realized by wrapping two pulley waveguides around the input and output sides of the ring [7]. This configuration essentially establishes two unbalanced MZIs, MZI1 and MZI2, out of the waveguides and the ring. AMZI1 (AMZI2) consists of two directional couplers with coupling ratios of k1 and k2 (k3 and k4) and two arms with lengths of l1 and l3 (l2 and l5). For our chip, we set k1=k2

and k3=k4. The radius of the ring is r, while the lengths l4 and l6 are from coupler to coupler. We suppose that the directional couplers have zero length and a wavelength-independent coupling ratio within the wavelength range of interest. If the waveguide lengths are properly chosen, the FSR of the MZIs can be twice that of the ring.

The transmission spectrum of the resonator can be analysed by using a combination of transfer matrices [8]. As shown in Supplementary Figure 4a, the resonators can be divided into two kinds of four-port blocks and two transmission waveguides, labelled as sections I, II and III. For each section, two basic units, the directional coupler and the transmission waveguides, can be expressed in matrix form, relating the input (E_{in1}, E_{in2}) and output (E_{out1}, E_{out2}):

$$\begin{pmatrix} E_{out1} \\ E_{out2} \end{pmatrix} = H \cdot \begin{pmatrix} E_{in1} \\ E_{in2} \end{pmatrix} = \begin{bmatrix} H_{11} & H_{12} \\ H_{21} & H_{22} \end{bmatrix} \cdot \begin{pmatrix} E_{in1} \\ E_{in2} \end{pmatrix} \tag{1}$$

For the directional coupler with a coupling ratio of κ, the transfer matrix is given as

$$H_\kappa = \gamma \begin{bmatrix} t & i\kappa \\ i\kappa & t \end{bmatrix}, \tag{2}$$

where i=$\sqrt{-1}$, t =$\sqrt{1 - \kappa^2}$and γ is the amplitude transmission coefficient of the coupler. For transmission waveguides with lengths of $l1$ and $l3$, we can define the transfer matrix as

$$H_{l_1,l_3} = \begin{bmatrix} e^{i(\beta+i\alpha)l_1} & 0 \\ 0 & e^{i(\beta+i\alpha)l_3} \end{bmatrix}, \tag{3}$$

where α is the waveguide transmission loss coefficient and β is the propagation constant. Hence, we derive the transfer matrix H_{C_1} for the cascaded components in section I as

$$H_{C_1} = H_{\kappa 2} \cdot H_{l_1,l_3} \cdot H_{\kappa 1}, \tag{4}$$

which gives

$$\begin{pmatrix} E_t \\ E_2 \end{pmatrix} = H_{C_1} \cdot \begin{pmatrix} E_i \\ E_1 \end{pmatrix}. \tag{5}$$

The same formulas can be used to derive the transfer matrix for section III, which relates the two input-output pairs (E_a,E_3)

and (E_d, E_4)

$$\begin{pmatrix} E_d \\ E_4 \end{pmatrix} = H_{C_2} \cdot \begin{pmatrix} E_a \\ E_3 \end{pmatrix}, \tag{6}$$

where

$$H_{C_2} = H_{\kappa 4} \cdot H_{l_2,l_5} \cdot H_{\kappa 3}. \tag{7}$$

The cascade of two-pair systems, section I and section III, involves recirculating light; it is feasible to use a chain matrix G to combine the input-output pairs as

$$\begin{pmatrix} E_i \\ E_t \end{pmatrix} = G_{C_1} \cdot \begin{pmatrix} E_2 \\ E_1 \end{pmatrix}, \tag{8}$$

and

$$\begin{pmatrix} E_4 \\ E_3 \end{pmatrix} = G_{C_2}^{-1} \cdot \begin{pmatrix} E_a \\ E_d \end{pmatrix}, \tag{9}$$

where the elements of G can be derived from the transfer matrix H by the following conversion formulas [9]

$$\begin{aligned} G_{11} &= 1/H_{21} \\ G_{12} &= -H_{22}/H_{21} \\ G_{21} &= H_{11}/H_{21} \\ G_{22} &= (H_{12}H_{21} - H_{11}H_{22})/H_{21}. \end{aligned} \tag{10}$$

Moreover, the relation between (E_3, E_4) and (E_2, E_1) in section II is only related to the transmission lengths l_4 and l_6,

$$\begin{pmatrix} E_2 \\ E_1 \end{pmatrix} = T_{-l_4,l_6} \cdot \begin{pmatrix} E_4 \\ E_3 \end{pmatrix} = \begin{bmatrix} 0 & e^{-i(\beta+i\alpha)*l_4} \\ e^{i(\beta+i\alpha)*l_6} & 0 \end{bmatrix} \cdot \begin{pmatrix} E_4 \\ E_3 \end{pmatrix} \tag{11}$$

Substituting Eqs. (9)-(11) in Eq. (8), one can relate the mixed input-output pairs (E_i, E_t) and (E_d, E_a) as

$$\begin{pmatrix} E_i \\ E_t \end{pmatrix} = G_T \cdot \begin{pmatrix} E_a \\ E_d \end{pmatrix}, \tag{12}$$

where

$$G_T = G_{C_1} \cdot T_{-l_4, l_6} \cdot G_{C_2}^{-1}. \tag{13}$$

Finally, the transfer matrix H_T from the input pair (E_i, E_a) to the output pair (E_d, E_t) can be determined from the elements of the chain matrix G_T by using the following formulas:

$$H_{11} = G_{21}/G_{11}$$

$$H_{12} = (G_{11}G_{22} - G_{12}G_{21})/G_{11}$$

$$H_{21} = 1/G_{11} \tag{14}$$

$$H_{22} = -G_{12}/G_{11}.$$

By considering E_a=0, the transmittance characteristics can be obtained as

$$E_d = \frac{\gamma^4 (t_1 \kappa_2 \varphi_1 + \kappa_1 t_2 \varphi_3) \varphi_4 (\kappa_3 t_4 \varphi_2 + t_3 \kappa_4 \varphi_5)}{1 - \gamma^4 (t_3 t_4 \varphi_5 - \kappa_3 \kappa_4 \varphi_2) \varphi_6 (t_1 t_2 \varphi_3 - \kappa_1 \kappa_2 \varphi_1) \varphi_4}, \tag{15}$$

and

$$E_t = \frac{\gamma^6 (t_3 t_4 \varphi_1 \varphi_3 \varphi_4 \varphi_5 \varphi_6 - \kappa_3 \kappa_4 \varphi_1 \varphi_2 \varphi_3 \varphi_4 \varphi_6) - \gamma^2 (t_1 t_2 \varphi_1 - \kappa_1 \kappa_2 \varphi_3)}{\gamma^4 (t_3 t_4 \varphi_5 - \kappa_3 \kappa_4 \varphi_2) \varphi_6 (t_1 t_2 \varphi_3 - \kappa_1 \kappa_2 \varphi_1) \varphi_4 - 1}, \tag{16}$$

where $\varphi_i = e^{-\alpha l_i} e^{i\theta_i}$, with $\theta_i = \beta l_i$ (i=1,2,3,4,5,6). It can be seen from Eqs. (15) and (16) that the phase term φ_i has a critical influence on the resonator transmission characteristics. Without loss of generality, we assume that the four phase terms for the ring are equal ($\varphi_3 = \varphi_4 = \varphi_5 = \varphi_6 = \varphi_r = \exp[-\alpha 2\pi r/4] \cdot \exp[i\beta 2\pi r/4]$). There are four distinct closed loops within the resonator, and the imposed resonance conditions for the round-trip phase delays are

$$\theta_1 + \theta_2 + 2\theta_r = N_1 \times \pi$$

$$\theta_1 + 3\theta_r = N_2 \times \pi$$

$$\theta_2 + 3\theta_r = N_3 \times \pi$$

$$4\theta_r = N_4 \times \pi.$$

(17)

Theoretical calculations of the pump transmittance characteristic of the DMZI-R with $2\alpha = 0.69\ cm^{-1}$ and a radius of 15 μm are shown in Supplementary Figure 4b versus the detuning phase ϕ_1 of AMZI1 for different detuning phases ϕ_2 of AMZI2, where $\phi_1 = \theta_1 - \theta_r$ and $\phi_2 = \theta_2 - \theta_r$. The length difference of the AMZI1 (AMZI2) is 47.8 μm (48 μm), corresponding to the nominally designed parameters of our chip. The input (output) side directional coupler amplitude coupling ratio is set to 0.25 (0.2) in the absence of coupling loss (γ=1). It can be seen from this figure that the phase matching conditions rely on the interference pattern of the input and output MZIs. At the input side $\phi_1 = 2N\pi$ ensures that the pump laser couples into the resonator, while at the output side $\phi_2 = (2N + 1)\pi$ minimizes the pump leakage from the drop port and hence maintains the pump within the ring and isolates the ring from photons exiting via the drop port. The phase matching conditions for the generated photons (signal and idler) in the ring are exactly opposite.

The tunable relative phase between the different paths can be realized by the PSs in our device. By appropriately choosing the coupling ratio of the directional coupler and applying heaters to the device, one can effectively achieve critical coupling for the pump photon and over-coupling for both the signal and idler photons.

Supplementary Figure 5 shows the transmission spectra of S1 from the add port to the drop port and from the input port to the through port before (a and b) and after (c and d) optimizing the heaters. From a comparison of Supplementary Figure 5a and 5c, we have enhanced the transmission from the add port to the drop port by tuning the phase of MZI2. Due to the complementary nature of the two-mode MZI, we can minimize the pump (indicated by "pump" in the figure) leakage from the ring into the drop port and hence maintain the pump within the ring for efficient SFWM. Moreover, at the wavelengths of the signal and idler photons (indicated with red and blue letters), the transmission increases; hence, the extraction efficiency of the correlated photon pair is also enhanced. On the other hand, from a comparison of Supplementary Figure 5b and 5d, by tuning the phase of MZI1, we reduce the transmission of the pump from the input port into the through port and hence maintain the pump within the ring for efficient SFWM. This design can greatly enhance the generation and extraction efficiency of the photon pairs simultaneously and reduce the amount of filtering needed for the pump. In addition, the design can also reduce the spurious SFWM pairs generated in the input waveguide if the coupler to the source is long and further improve the signal-to-noise ratio.

According to the optimum heater configuration that exhibits the desired spectral dependence shown in Supplementary Figure 5, we characterize the coincidence counts of S1 in detail. Supplementary Figure 6a shows the through-through (T-T) coincidence results upon performing a 2-D sweep of the current across the heaters above MZI1 and MZI2 for the on-resonance (black dots) and off-resonance (blue dots) cases, respectively. The average pump power is set to be 0.13 mW before coupling into the chip. We find that in the off-resonance case, the coincidence counts of T-T do not change with the modulation currents. The high rate in the off-resonance case is a result of broadband SFWM in the input bus waveguide, which will be discussed in the following paragraphs. On resonance, the coincidence counts strongly depend on the settings of MZI1 and MZI2 mainly because some of the pump light is coupled into the ring, resulting in less photon pair generation in the straight waveguide. In addition, the T-T coincidence counts cannot be reduced to zero because the photon pairs generated in the input waveguide before the source will be completely outcoupled from the through port when MZI1 is tuned to only support the pump photon at the input side. The drop-drop (D-D) coincidence counts are shown in Supplementary Figure 6b. Off-resonance, D-D dose not show a coincidence count since the pump is not coupled into the ring. For the on-resonance case, as the scan current gradually approaches the optimal configurations, the coincidence counts constantly increase, which complements the on-resonance case of T-T compared to Supplementary Figure 6a. Supplementary Figure 6c illustrates the coincidence counts of Ds-Di, Ds-Ti and Ts-Di as a function of the average pump power. The D-D coincidence rate increases with power, because the efficiency of SFWM scales quadratically with the pump power. The measured rate is 570 Hz at a pump power of 0.275 mW. Taking into account the losses of each photon (fibre-chip-fibre losses of 15.56 dB, insertion losses of the off-chip WDMs of 2.2 dB, and detection losses of 0.97 dB), the inferred generation rate is approximately 3.2 MHz in the resonator. The inset of Supplementary Figure 6c shows that the coincidence efficiency changes with the average pump power. To remove the effect of the photon generation from the input waveguide, we only use the drop port coincidences Ds-Di and split coincidences Ds-Ti and Ts-Di to deduce the coincidence efficiency [7]:

$$Coincidence \quad efficiency = \frac{CC_{Ds-Di}^2}{\left(CC_{Ds-Di} + \frac{CC_{Ds-Ti} + CC_{Ts-Di}}{2}\right)^2}. \tag{18}$$

As shown in the inset, in the case of low pump power, the coincidence efficiency is 0.97; however, as the power increases, i.e., as the coincidence rate of Ds-Ti and Ts-Di increases, the efficiency gradually decreases, which results from the accidental rate as shown in Supplementary Figure 6d. All the peaks in the histogram of the Ds-Ti and Ts-Di coincidences are similar, while in the case of D-D, the accidental peaks are almost not visible compared to the main peak. The peaks with a time interval of 16 ns correspond to the simultaneous detection of photons from different pump pulses.

To illustrate the broadband SFWM in the bus waveguide, we measure the continuous emission spectra for the signal and idler

photons with the currents set to the on-resonance conditions. In the experimental setup shown in Supplementary Figure 7a, a pulsed laser with an average power of 0.13 mW is first filtered by 200 GHz cascade dense WDM (DWDM) filters to remove the background noise and then is coupled into the chip. Photon pairs are generated from the chip through SFWM, and the photons coupling out from the chip are filtered by a multi-channel 100 GHz DWDM. Supplementary Figure 7c shows the single-count rates for different channels, with a maximum wavelength interval from the pump of approximately 8.5 nm. The rates without filtering loss are inferred based on the independently measured insertion losses for each channel shown in Supplementary Figure 7b. The differences in the single-count rates mainly arise from the Raman scattering of the signal and idler channels. The coincidence rates of the channel pairs are recorded and shown in Supplementary Figure 7d. It is clear that the spectrum of the SFWM in the input waveguide is substantially wider than that of the resonance-matched DMZI-R.

Optimization of two-qubit entanglement

Supplementary Figure 8a to 8c show the two-qubit correlation curves with variations in the interference fringes, i.e., visibilities (b), and phase variations (c) between the different interference curves as a function of the S3-to-S1 detuning. Supplementary Figure 8d to 8f show the corresponding results of the S3-to-S2 detuning. To maintain the matching conditions between MZI1, MZI2 and the ring, we simultaneously change the three heaters on the scanned source with a step of 0.1 mW. It is clear that when the sources are largely detuned, no obvious interference occurs. As the spectra of the sources gradually match, clear interference patterns can be observed. In Supplementary Figure 8c and 8f, the phase variations between the different interference curves are almost linear with approximately the same dependence on the source scanning power, approximately $\frac{10\pi}{3}mW^{-1}$. Therefore, if there is non-negligible thermal or electrical crosstalk mismatching the spectra of the sources, the initial phase of the interference curves will change.

In Supplementary Figure 9, the fringes, visibilities and phase variations between the different path correlation curves for S1 and S3 (a-c) and S2 and S3 (d-f) are plotted for different pump power splittings between the sources while setting the sources detuning power to 0. The step of the heating power applied to P_{y1} or P_{y2} is 1 mW, and the phase change is approximately 0.048π. As can be seen from a and d, the interference curves exhibit a significant dependence on the balance of the photon-pair emission between the sources, which can be used to control the amplitude between the components of the output state to prepare variably entangled states. When a maximally entangled state is produced, the maximum visibility can be observed in b and e (94.72%±0.50% for S1 and S3, 96.10%±0.40% for S2 and S3, respectively). It is also worth noting that the phase variations shown in c and f nearly do not change as the balance changes, indicating that the scanned PS has little impact on the resonator-based sources, since changes in the spectra overlap, i.e., resonance shifts between the sources can introduce a relative phase between the two-qubit state, as shown in Supplementary Figure 8. This shows that the electrical and thermal crosstalk are

effectively isolated.

Two-qutrit correlation space

Generally, for a two-qutrit system, the entangled state can be written as

$$\Psi = (\alpha \exp^{i2\varphi_{pz1}} |00\rangle + \beta \exp^{i2\varphi_{pz2}} |11\rangle + \gamma |22\rangle). \tag{19}$$

A complete characterization of the higher-order two-qutrit correlations can be realized by using two three-dimensional multiports (3D-MPs). After each qutrit enters the 3D-MP, the state is transformed by a local unitary transformation ($\mathbb{U}$):

$$\mathbb{U} = \frac{1}{3} \begin{pmatrix} 1 & 1 & 1 \\ 1 & e^{i\frac{2\pi}{3}} & e^{-i\frac{2\pi}{3}} \\ 1 & e^{-i\frac{2\pi}{3}} & e^{i\frac{2\pi}{3}} \end{pmatrix} \otimes \begin{pmatrix} 1 & 1 & 1 \\ 1 & e^{i\frac{2\pi}{3}} & e^{-i\frac{2\pi}{3}} \\ 1 & e^{-i\frac{2\pi}{3}} & e^{i\frac{2\pi}{3}} \end{pmatrix} \tag{20}$$

Then, the resulting state can be written as

$$\begin{aligned} |\Psi^{'}\rangle &= U |\Psi\rangle \\ &= \frac{1}{3}\alpha e^{i2\varphi_{pz1}} \left| \begin{matrix} 1 \\ 1 \\ 1 \end{matrix} \right\rangle \otimes \left| \begin{matrix} 1 \\ 1 \\ 1 \end{matrix} \right\rangle + \frac{1}{3}\beta e^{i2\varphi_{pz2}} \left| \begin{matrix} 1 \\ e^{i2\pi/3} \\ e^{-i2\pi/3} \end{matrix} \right\rangle \otimes \left| \begin{matrix} 1 \\ e^{i2\pi/3} \\ e^{-i2\pi/3} \end{matrix} \right\rangle + \frac{1}{3}\gamma \left| \begin{matrix} 1 \\ e^{-i2\pi/3} \\ e^{-i2\pi/3} \end{matrix} \right\rangle \otimes \left| \begin{matrix} 1 \\ e^{-i2\pi/3} \\ e^{-i2\pi/3} \end{matrix} \right\rangle \end{aligned} \tag{21}$$

The probabilities of detecting a photon pair for different detector combinations are:

$$\begin{aligned} P_{12} = P_{36} = P_{54} &= \frac{1}{9}\left| \alpha e^{i(2\varphi_{pz1}+\frac{2\pi}{3})} + \beta e^{i(2\varphi_{pz2}-\frac{2\pi}{3})} + \gamma \right|^2 \\ P_{14} = P_{32} = P_{56} &= \frac{1}{9}\left| \alpha e^{i2\varphi_{pz1}} + \beta e^{i2\varphi_{pz2}} + \gamma \right|^2 \\ P_{16} = P_{34} = P_{52} &= \frac{1}{9}\left| \alpha e^{i(2\varphi_{pz1}-\frac{2\pi}{3})} + \beta e^{i(2\varphi_{pz2}+\frac{2\pi}{3})} + \gamma \right|^2. \end{aligned} \tag{22}$$

In the experiment, we set $\alpha = \beta = \gamma = \frac{1}{\sqrt{3}}$ and adjust the relative pump phase over S1 and S2 to characterize the high-order Einstein-Podolsky-Rosen (EPR) correlations. All nine output combinations of the coincidences and their respective theoretical results are shown in Supplementary Figure 10. Due to the symmetry of the multi-mode interferometers, three probabilities P_{ij} of equal values are observed. For each pattern, there are three repeated results for each correlation pattern, and the experimental results are in good agreement with the theoretical results.

Supplementary References

[1] W. Bogaerts, P. De Heyn, T. Van Vaerenbergh, K. De Vos, S. Kumar Selvaraja, T. Claes, P. Dumon, P. Bienstman, D. Van Thourhout, and R. Baets, Laser Photonics Rev. **6**, 47 (2012).

[2] J. Carolan, C. Harrold, C. Sparrow, E. Martín-López, N. J. Russell, J. W. Silverstone, P. J. Shadbolt, N. Matsuda, M. Oguma, M. Itoh, et al., Science **349**, 711 (2015).

[3] S. Paesani, A. A. Gentile, R. Santagati, J. Wang, N. Wiebe, D. P. Tew, J. L. OBrien, and M. G. Thompson, Phys. Rev. Lett. **118**, 100503 (2017).

[4] J. W. Silverstone, R. Santagati, D. Bonneau, M. J. Strain, M. Sorel, J. L. OBrien, and M. G. Thompson, Nat. Commun. **6**, 7948 (2015).

[5] X. Qiang, X. Zhou, J. Wang, C. M. Wilkes, T. Loke, S. OGara, L. Kling, G. D. Marshall, R. Santagati, T. C. Ralph, et al., Nat. Photon. **12**, 534 (2018).

[6] N. C. Harris, Y. Ma, J. Mower, T. Baehr-Jones, D. Englund, M. Hochberg, and C. Galland, Opt. Express **22**, 10487 (2014).

[7] C. Tison, J. Steidle, M. Fanto, Z. Wang, N. Mogent, A. Rizzo, S. Preble, and P. Alsing, Opt. Express **25**, 33088 (2017).

[8] G. Barbarossa, A. M. Matteo, and M. N. Armenise, IEEE J. Lightwave Technol. **13**, 148 (1995).

[9] B. Moslehi, J. W. Goodman, M. Tur, and H. J. Shaw, Proc. IEEE **72**, 909 (1984).
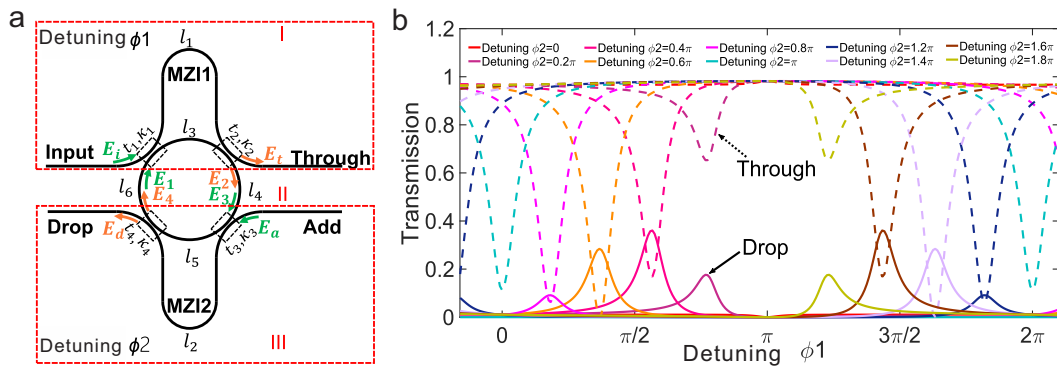
Supplementary figures
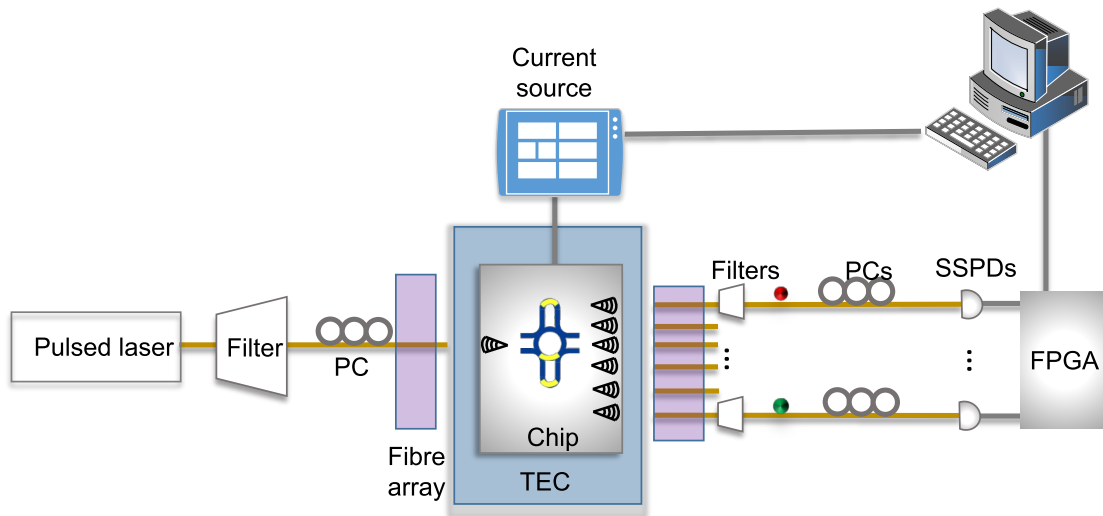
Supplementary Figure 1: Schematic of the experimental setup. BS: beam splitter; PC: polarization controller; PID: proportional integrative derivative; SSPD: superconducting nanowire single photon detector; TEC: temperature controller; FPGA: field-programmable gate array.
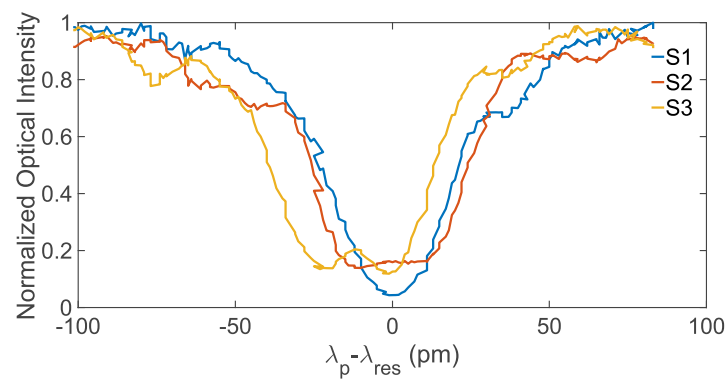

Supplementary Figure 2: Spectral profiles of the micro-ring resonator sources. The full widths at half maximum (Q-factor) of $S1$, $S2$ and $S3$ are approximately 44 pm (3.5×10^4), 50 pm (3.1×10^4) and 53 pm (2.9×10^4), respectively. All the sources are observed to be largely spectrally indistinguishable.
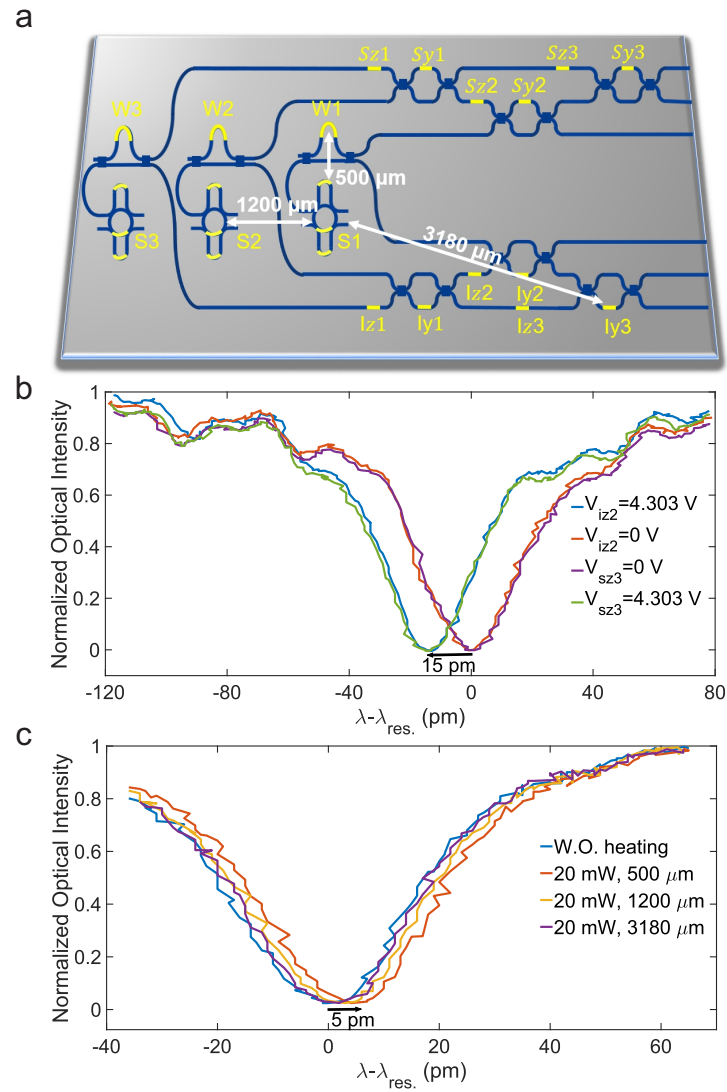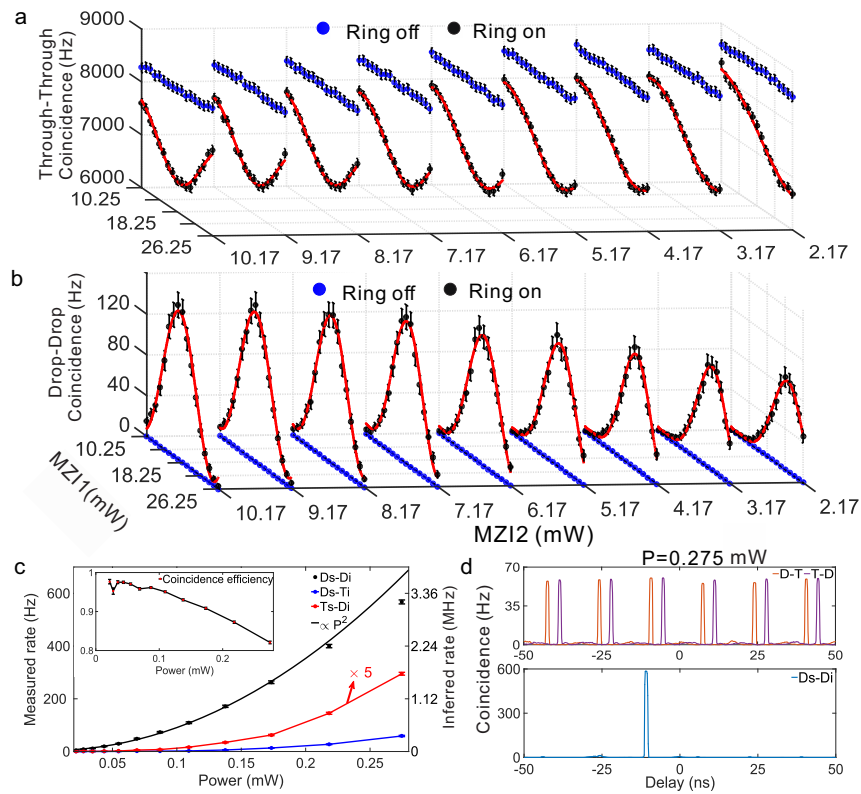
Supplementary Figure 3: Characterization of the electric and thermal crosstalk of S1 on our chip. **a.** Schematic of the chip. **b.** The resonance of the source shifts 15 pm from its off position when 4.303 V is applied to the PS (φ_{iz2} or φ_{sz3}). **c.** The thermal crosstalk is characterized by applying 20 mW of heating power to the PSs with different distances to the source. An obvious blueshift is observed for a small distance due to the heat dissipation.
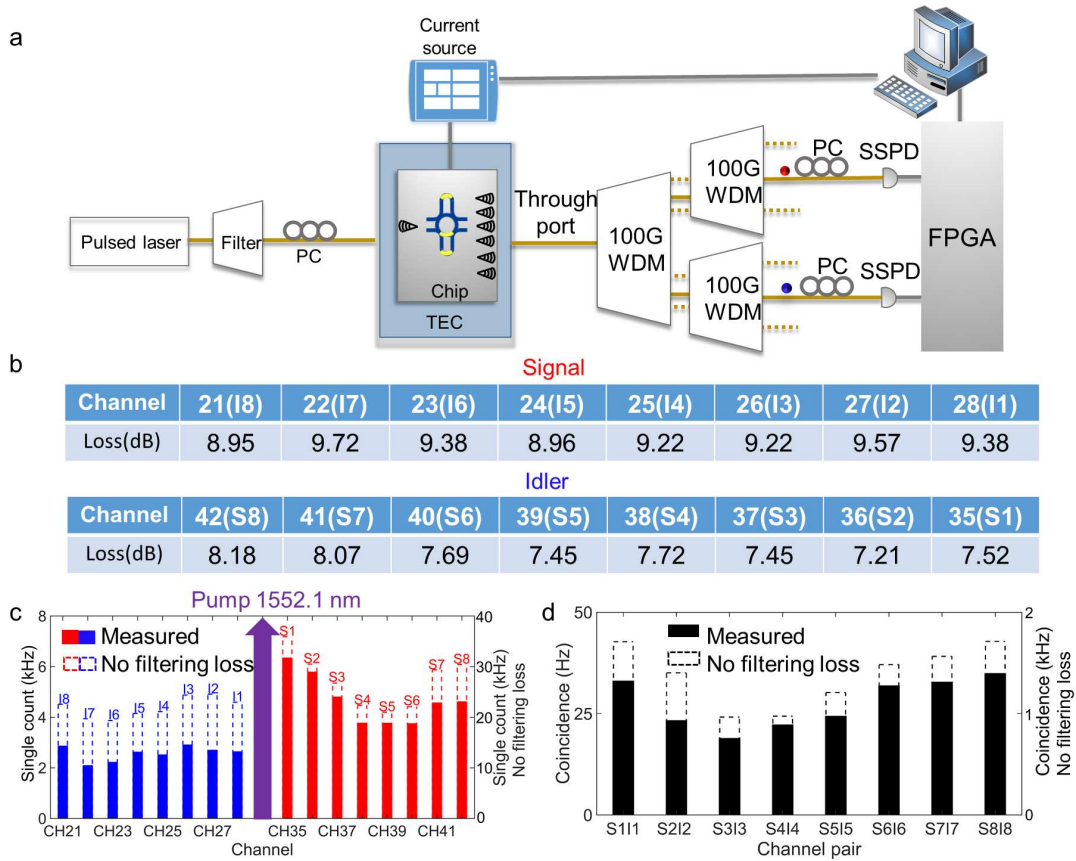
Supplementary Figure 4: **a.** Schematic diagram of a DMZI-R. **b.** Theoretical calculations of the pump transmittance characteristics of the through port (dashed lines) and drop port (solid lines) with a attenuation coefficient $2\alpha = 0.69 \ cm^{-1}$ for a ring with $r=15 \ \mu m$ versus of the detuning phase of the AMZI at the input side for different detuning phases of the AMZI at the output side.
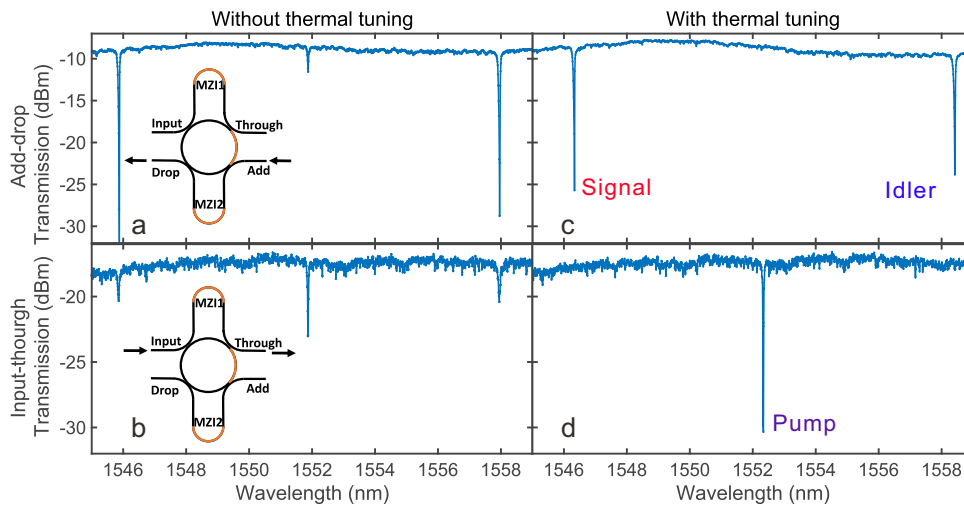
Supplementary Figure 5: Spectrum characterization of the DMZI-R. Transmission spectra from the add port to the drop port and input port to the through port: **a.** add port to the drop port without thermal tuning; **b.** input port to the through port without thermal tuning; **c.** add port to the drop port with thermal tuning and **d.** input port to the through port with thermal tuning. The insets show a schematic diagram of the measurement.

Supplementary Figure 6: Characterization of S1. **a.** The through-through ports coincidence results of the on-resonance (black dots) and off-resonance (blue dots) cases upon performing a 2-D sweep of the current across the heaters above MZI1 and MZI2 with an average pump power of 0.13 mW before coupling into the chip. It is clear that in the on-resonant case, the coincidence counts depend strongly on the settings of the PSs of MZI1 and MZI2. However, the minimum of the interference fringe is high. Moreover, if we tune the ring to be off resonant with the pump, phase-independent coincidence counts are obtained, as shown by the blue data points. The high rate in the off-resonance case is a result of broadband SFWM in the input bus waveguide. **b.** 2-D sweep coincidence results of the drop-drop ports. In the off-resonance (blue dots) case, eliminating the possibility of photon pair generation within the resonator, the coincidence counts are approximately equal to zero. If the pump laser is tuned to be resonant (black dots), the settings of MZI1 and MZI2 have a significant effect on the drop port coincidences, depending on how efficiently the pump is coupled into the resonator. **c.** Coincidence rate of different ports as a function of the average pump power. The dashed line is a quadratic fit. The inset shows that the coincidence efficiency changes with the average pump power. The points are experimental data, and the curves are fits. All the data are raw counts and no background counts are subtracted. The error bars are calculated by a Poissonian distribution. Since the Ds-Ti and Ts-Di lines are approximately overlapped, we multiply Ts-Di by five times to guide the eye. **d.** A typical histogram of the coincidence measurements at an input average pump power of 0.275 mW at different ports. This result shows the excellent signal-to-noise ratio of the DMZI-R source.

Supplementary Figure 7: Characterization of the broadband SFWM in the input bus waveguide at the through port of the source. **a.** Schematic of the experimental setup. **b.** Measured losses of the multi-channel 100 GHz WDM. **c.** Single-count rate spectra of the signal and idler photons filtered by the WDM for the measured case and the case without filtering loss. **d.** The measured and inferred coincidence rates of the channel pair.
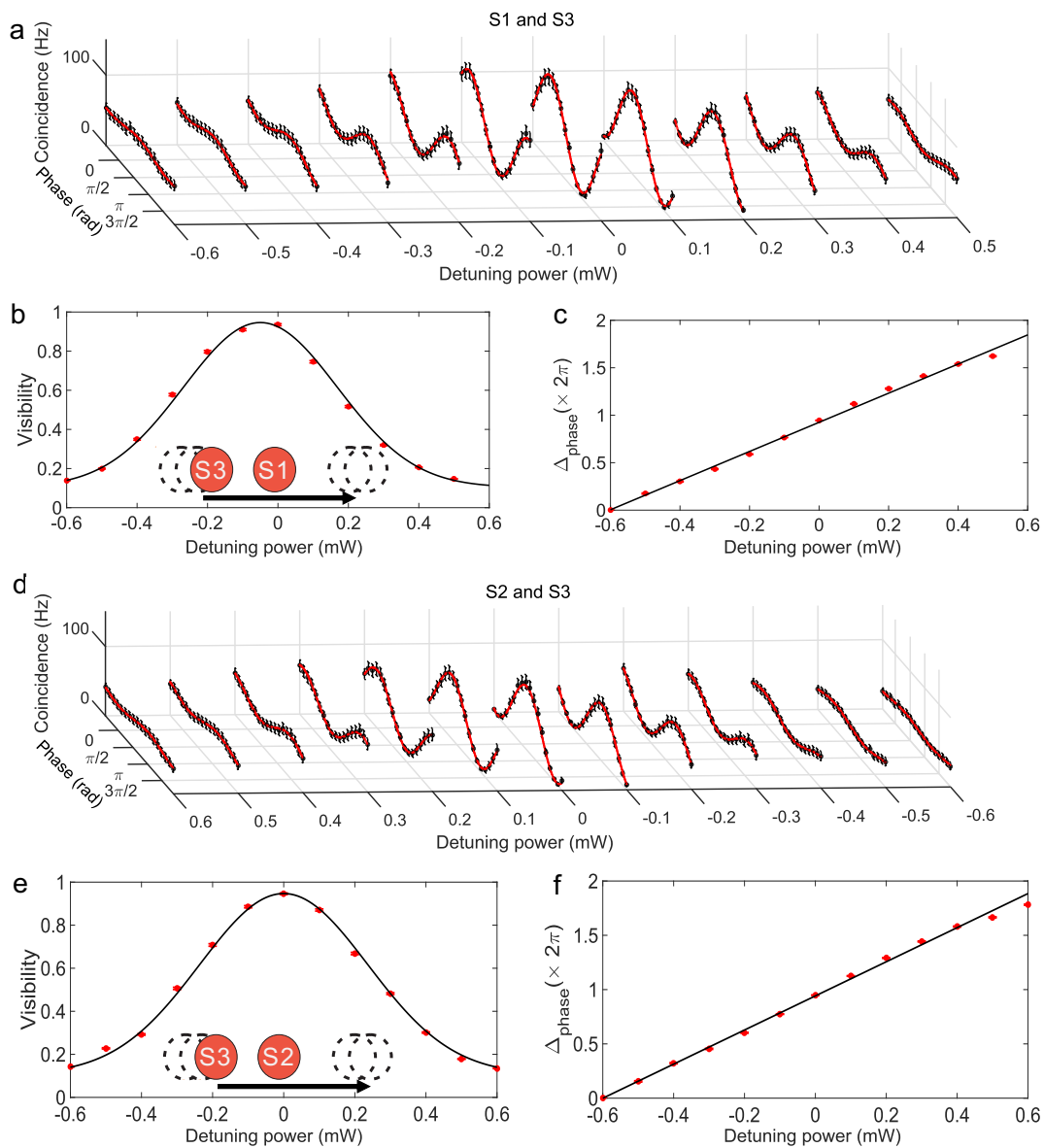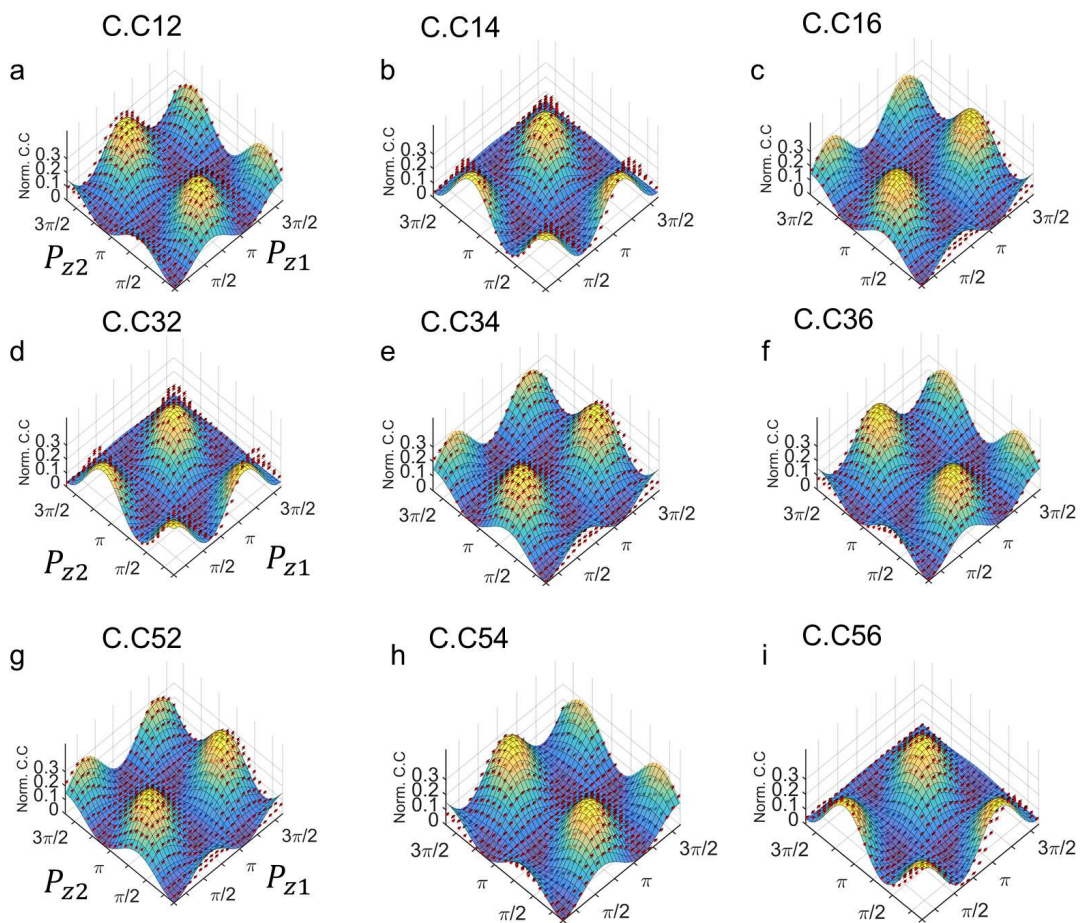
Supplementary Figure 8: Path correlations results for S1 and S3 and S2 and S3 as one source resonance is swept over the other. Two-qubit correlation curves (**a/d**), changes in the two-qubit path interference visibilities (**b/e**) and phase variations between the different interference curves (**c/f**) are measured as S3 is scanned over S1/S2 with a step of 0.1 mW. The error bars are calculated by a Poissonian distribution. The red dots are the measured data, and the curves are drawn to guide the eye.
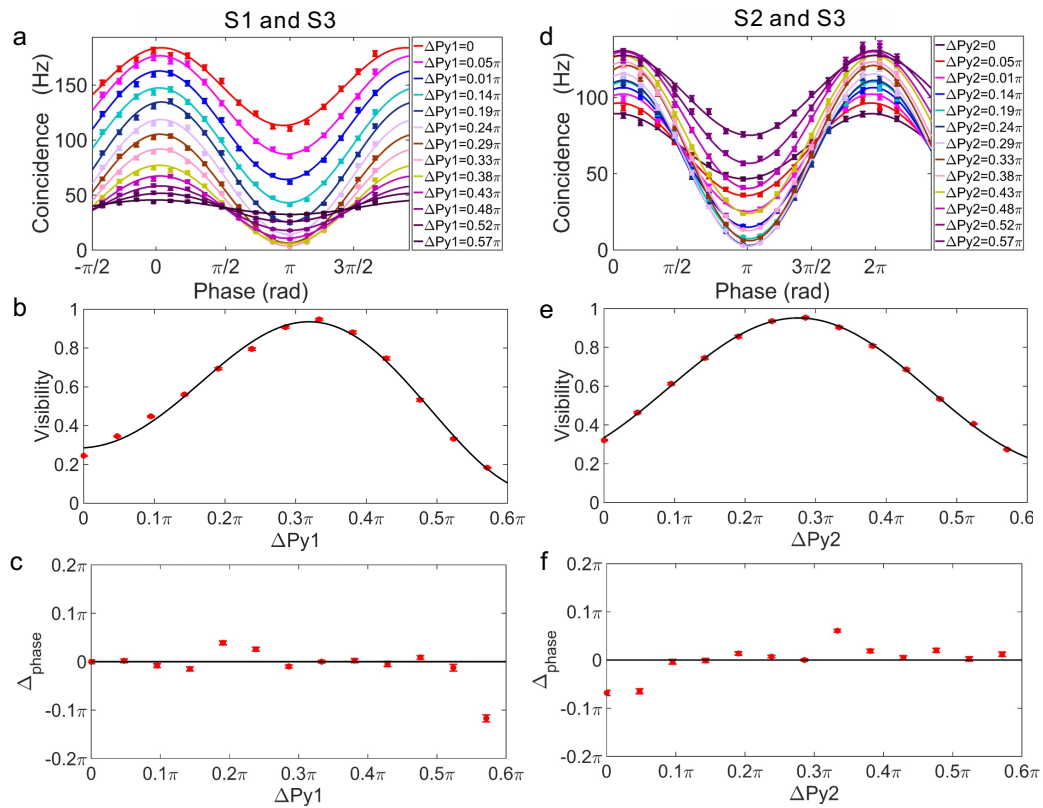
Supplementary Figure 9: Path correlations for S1 and S3 (a-c) and S2 and S3 (d-f), obtained for different current conditions (with a 1 mW step) applied to P_{y1} and P_{y2}, used as a pump power splitter to balance the generation rate between the measured sources. The interference fringes (**a,d**), visibilities (**b,e**) and changes in the initial phase between the different interference curves (**c,f**) are shown for different pump power splitting ratios. The error bars are calculated by a Poissonian distribution. The points represent the experimental data, and the curves are fitted to guide the eye.

Supplementary Figure 10: Full scan of the correlation space for two entangled qutrits state $|\Psi\rangle = \frac{1}{\sqrt{3}}(e^{i2\varphi_{pz1}}|00\rangle + e^{i2\varphi_{pz2}}|11\rangle + |22\rangle)$. Figures **a** to **i** correspond to detector combinations of (1,2), (1,4), (1,6), (3,2), (3,4), (3,6), (5,2), (5,4), and (5,6) respectively, while two relative pump phases φ_{pz1} and φ_{pz2} are scanned. The error bars are calculated by a Poissonian distribution. The normalized measured coincidences (Norm. C.C) (red dots) and simulated results (lines) are compared and show excellent agreement with each other.